J Oceanogr (2016) 72:23–37
DOI 10.1007/s10872-015-0320-6

SPECIAL SECTION: ORIGINAL ARTICLE

Oceanographic observations after the 2011 earthquake off the Pacific coast of Tohoku

Fine-scale structure and mixing across the front between the Tsugaru Warm and Oyashio Currents in summer along the Sanriku Coast, east of Japan

Sachihiko Itoh[1] · Hitoshi Kaneko[1] · Miho Ishizu[1] · Daigo Yanagimoto[1] · Takeshi Okunishi[2] · Hajime Nishigaki[3] · Kiyoshi Tanaka[1]

Received: 18 December 2014 / Revised: 29 July 2015 / Accepted: 15 August 2015 / Published online: 21 September 2015

Abstract High-resolution shipboard observations were made across the front between the Tsugaru Warm Current (TWC) and the Oyashio Current in July 2013. Fine structure in the frontal zones was successfully captured with an underway conductivity–temperature–depth profiler deployed with a typical horizontal interval of 2–3 nautical miles. The front characterized by marked horizontal gradients in temperature and salinity extended from the subsurface onto the shelf. Along this frontal layer, the minimum frequency for internal waves became substantially lower than the local inertial frequency, mainly due to the strong vertical shear of the geostrophic velocity. Turbulent energy dissipation rates ε (vertical diffusivity K_ρ) were frequently elevated along the front and its offshore side up to 3×10^{-8} W kg^{-1} (10^{-4} m^2 s^{-1}), which may have been caused by an "internal tide chimney", trapping low-frequency internal waves within the band of strong shear. At the onshore side of the TWC on the shelf, strong mixing with ε (K_ρ) exceeding 10^{-6} W kg^{-1} (10^{-3} m^2 s^{-1}) was also observed. A large portion of the water columns in the frontal area provided suitable conditions for double diffusion; in some layers with moderate turbulence, temperature microstructures indicative of double diffusion were observed. The vigorous mixing processes around the front are likely to modify the properties of the TWC downstream, which could then produce a latitudinal gradient in environments along the coast.

Keywords Tsugaru Warm Current · Oyashio (Oyashio Current) · Front · Vertical mixing · Internal tide chimney · 2011 off the Pacific coast of Tohoku earthquake · The Great East Japan earthquake

1 Introduction

The Tsugaru Warm Current (TWC) is an outflow from the Sea of Japan through the Tsugaru Strait into the subtropical–subarctic transition zone of the North Pacific (Fig. 1). It is connected to the subtropical gyre through the Tsushima Warm Current in the Sea of Japan (Yasuda 2003). In areas around the path of the TWC, the relatively warm water originating from the subtropical gyre has major impacts on the local climate, ecosystems, and fisheries. The influence is often clear along the Sanriku Coast, south of the Tsugaru Strait, where the coastal branch of the Oyashio Current (OY) frequently occurs (Shimizu et al. 2001; Itoh and Sugimoto 2002), transporting cold subarctic waters from the north (Fig. 1). While the TWC takes the bimodal paths of the gyre and coastal modes (Conlon 1982; Yasuda et al. 1988), the net outflow from the strait is usually observed as a southward flow along the coast.

The OY water is generally rich in nutrients and phytoplankton, while it is significantly colder than the TWC. For some organisms living in inshore areas that are usually covered with TWC water, the invasion of the extremely cold OY shrinks their habitat areas and often increases mortality. However, when the TWC is sufficiently strong, it prevents OY water from reaching inshore areas. Instead, a boundary

✉ Sachihiko Itoh
itohsach@aori.u-tokyo.ac.jp

1 Atmosphere and Ocean Research Institute, The University of Tokyo, 5-1-5 Kashiwanoha, Kashiwa, Chiba 277-8564, Japan

2 Tohoku National Fisheries Research Institute, Fisheries Research Agency, Shiogama, Japan

3 Faculty of Education and Welfare Science, Oita University, Oita, Japan

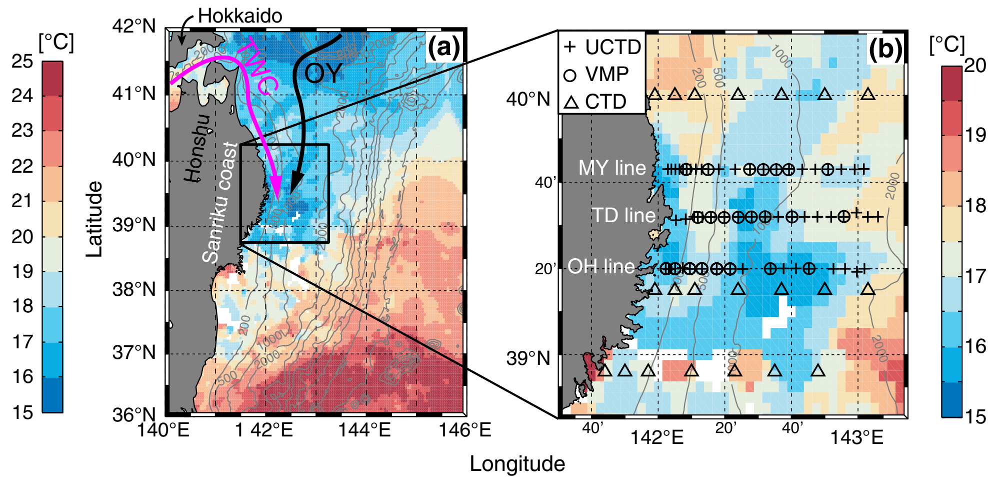

Fig. 1 Geographic and hydrographic features **a** east of Japan and **b** in areas off the Sanriku Coast. Bottom topography is shown as *gray contours* and sea surface temperature in early July 2013 is shown with *color shading*. **b** Observation stations for an underway conductivity–temperature–depth (UCTD) profiler (present study), a vertical microstructure profiler (VMP; present study) and a conductivity–temperature–depth profiler (CTD: observations taken by the Iwate Fisheries Technology Center) are shown with *crosses*, *circles* and *triangles*, respectively

between the two different water masses is formed on the shelf. This frontal area on the shelf is known as a good fishing ground for North Pacific giant octopus, hair crab and other demersal fishes.

The TWC and OY waters, together with the water from the Kuroshio Current flowing south of this area, are distinct sources for the upper layer waters off the Sanriku Coast. Based on temperature and salinity data, Hanawa and Mitsudera (1987) divided the water types observed in this area into six groups (termed "water systems" in their study). While two of them were assigned to generic surface and deep water systems, the other four were assumed to correspond to the TWC, the OY (ordinary OY and the extremely cold type referred to as coastal Oyashio) and the Kuroshio water systems. As noted in their study, however, this does not mean that water properties observed on specific occasions and locations are under the influence of a single source of water. The surface water is directly influenced by the atmosphere, which significantly modifies temperature and salinity values. In addition, horizontal and vertical mixing may play a role, especially around the frontal area.

Enhanced vertical mixing around fronts of western and eastern boundary currents of subtropical gyres has been the subject of much recent research based on observations, theoretical analyses, and numerical experiments (D'Asaro et al. 2011; Inoue et al. 2010; Kaneko et al. 2012; Johnston et al. 2011; Nagai et al. 2009, 2012; Rainville and Pinkel 2004; Whitt and Thomas 2013; Zhai et al. 2010). It has been suggested that the intensified mixing has significant impacts on new production through the supply of nitrate to the photic zone (Johnston et al. 2011; Kaneko et al. 2013). The mechanism of the enhancement has been attributed to near-inertial internal waves (e.g., Whitt and Thomas 2013) and/or symmetric instability (e.g., D'Asaro et al. 2011) that does not require the intervention of internal waves.

As shown in Kunze (1985), relative vorticity and vertical shear of geostrophic velocity alter the dispersion relationship of near-inertial internal waves through changing the effective inertial and buoyancy frequencies, respectively. In a strong baroclinic current, the minimum frequency for internal waves in geostrophic shear is approximated by Whitt and Thomas (2013) as (their Eq. 19)

$$\omega_{\min} = f\sqrt{1 + \mathrm{Ro} - \mathrm{Ri}^{-1}}, \tag{1}$$

where Rossby number $\mathrm{Ro} = \zeta_g/f$ is the relative vorticity of the geostrophic field normalized by the inertial frequency (and, hence, can be negative), and Ri is the gradient Richardson number calculated from the geostrophic velocity. It is noted that Ro generally changes the sign across the stream due to the contribution of the shear vorticity, while Ri is always positive. If $\omega_{\min} < f$ in a frontal layer and $\omega_{\min} = f$ in neighboring layers, internal waves with a frequency $\omega_{\min} \le \omega < f$ can only exist in the frontal layer. Furthermore, if there is an energy input with a frequency $\omega_{\min} \le \omega < f$ to this layer, internal waves at this frequency are excited but trapped within the area. This is likely to amplify these sub-inertial internal waves and result in their breaking (Whitt and Thomas 2013).

Because Eq. (1) was derived assuming the Wentzel, Kramers, and Brillouin (WKB) approximation, it is based on the assumption that wave scales are much smaller than the flow scale, which is usually not the case in a strong baroclinic current. Nevertheless, Whitt and Thomas

(2013) confirmed that the analytical solutions by the WKB approximation were consistent with results of the numerical experiments. Kunze (1985) also compared the results of the WKB-based ray tracing and numerical experiments, and concluded the two results qualitatively agreed if flow scales are not much smaller than wave scales. Thus, Eq. (1) is applicable to internal waves incident upon the front between the TWC and the OY, if the wave scale is not greater than the front scale.

The front between the TWC and the OY off the Sanriku Coast is different from those formed in western (such as the Kuroshio and the Gulf Stream) and eastern boundary currents (such as the California Current) mentioned above, in that pycnoclines between the two water masses are slanted toward the bottom. Therefore, the frontal structure may affect not only pelagic organisms but also the benthic ecosystem on the shelf. Moreover, tidally driven internal waves generated on the shelf could be more susceptible to interaction with the front between the TWC and the OY because it extends closer to the bottom than in previous studies such as of the Kuroshio front (Kaneko et al. 2012; Nagai et al. 2009, 2012).

Although seasonal hydrographic observations off the Sanriku Coast have often detected the front between the TWC and the OY (e.g., Wagawa et al. 2015), its detailed structure and dynamics (including mixing processes) have yet to be established. This is mainly because the existing data were not necessarily measured at a horizontal resolution high enough to capture the detailed frontal structure. As for the microstructure data required to estimate the vertical mixing intensity, Inoue et al. (2007), conducted measurements in areas south of Hokkaido, but no data were available for the area off the Sanriku Coast.

The importance of observations for the environments off the Sanriku Coast increased further after the March 11, 2011 earthquake off the Pacific coast of Tohoku, when the mega tsunami caused catastrophic damage to communities and ecosystems along the Sanriku Coast. Since then, marine science activity in this area is expected to contribute to the reconstruction and development of the fisheries industry and to our understanding of ecosystem recovery processes.

In the present study, we aim to improve our understanding of the frontal structure between the TWC and the OY. High horizontal-resolution observations were carried out to obtain vertical profiles of temperature, salinity, and horizontal velocity across the front. Microstructure measurements were also conducted for selected stations around the front.

2 Materials and methods

Hydrographic surveys for the frontal area off the Sanriku Coast were carried out during research cruise KK-13-2 aboard the R/V *Daisan Kaiyo Maru* from July 5 to 11, 2013. Observations of the frontal structure were taken along three east–west transects at latitudes of 39°43′N (off Miyako Bay: MY line), 39°32′N (off Point Todogasaki: TD line) and 39°20′N (off Point Ohakozaki: OH line) (Fig. 1b) from July 8 to 10. The TD line overlapped with those of monthly hydrographic observations carried out by the Iwate Prefecture Fisheries Technology Center (Wagawa et al. 2015). Our observation lines extend offshore from the coast with lengths of approximately 1° longitude (~ 86 km).

For each of the three lines, vertical profiles of temperature and salinity were first obtained with an UCTD measurement system (Rudnick and Klinke 2007; UC-PRO, OceanScience Ltd.) from east to west, and then microstructure was measured with a VMP (Turbo VMP, Rockland Scientific International Inc.) from west to east for selected stations (Fig. 1b; deployment time of the VMP was 30 min to 18 h after the UCTD probe deployment at the same station). UCTD observations were carried out down to 500 m or the near bottom layer (the UCTD probe was deployed so as not to touch the bottom), whichever was shallower, with a typical horizontal interval of 3 nautical miles (~5.6 km) in areas deeper than 200 m depth, and <2 nautical miles (~3.7 km) in areas shallower than 200 m depth. The ship speed was approximately 6 knots (~11 km h^{-1}) in areas deeper than 200 m depth, and 3 knots (~5.6 km h^{-1}) in areas shallower than 200 m depth. Note that two UCTD profiles along the MY line were not available due to deployment problems.

The VMP had integrated conductivity, temperature and pressure sensors. We attached two high-resolution velocity shear probes (SPM-38, Rockland Scientific International Inc.) and one high-resolution thermistor (FP07-38, Rockland Scientific International Inc.) to the VMP and made free-fall deployments with a tether of 500 m. Vertical profiles of horizontal velocity were continuously measured with a shipboard acoustic Doppler current profiler (Ocean Surveyor 75 kHz, Teledyne RDI) from 24 to 648 m depth with an interval of 16 m. Doppler data acquired during the UCTD observations from east to west, when the ship mostly steamed with a constant speed, were used to represent velocity profiles along each of the lines.

The raw UCTD data were processed with DataProcessing-Win32 software (Sea-Bird Electronics Inc.) to obtain temperature and salinity profiles at 1-m intervals. Potential density and potential temperature were then calculated. The raw VMP velocity shear data were processed using the Ocean Data Acquisition System (ODAS) Matlab Library provided by the manufacturer, which calculates turbulent energy dissipation rates ε from shear spectra. The detailed procedure was basically the same as that described in Itoh et al. (2010). We selected the bin length for calculating the spectra as 8 s, resulting in an approximate effective vertical resolution of energy dissipation rate profiles ranging from 5 to 7 m. Vertical diffusivity K_ρ was calculated from ε assuming mixing efficiency $\Gamma = 0.2$ (Osborn 1980),

$$K_\rho = \frac{\Gamma\varepsilon}{N^2} \tag{2}$$

where buoyancy frequency N was calculated from potential density σ_θ based on the simultaneous conductivity and temperature profiles as

$$N = \left(-\frac{g}{\rho_0}\frac{\partial\overline{\sigma_\theta}}{\partial z}\right)^{1/2}. \tag{3}$$

Note that the potential density profiles were smoothed with a 21-point (21 m) running mean, as indicated by an overbar (hereinafter used to indicate a 21-point running mean). Profiles referred to in the text below as smoothed are all smoothed in this way.

For the acoustic doppler current profiler (ADCP) velocity data, alignment errors were first removed from 1-min averaged data based on the method proposed by Joyce (1989). Then, erroneous data with quality (percent good) <90 %, those with error velocity magnitude exceeding 0.1 m s^{-1}, and those obtained during periods when the ship was accelerating, decelerating or changing direction were eliminated.

The vertical shear of ADCP horizontal velocity ($\partial u/\partial z$, $\partial v/\partial z$) was calculated between the mid-points of two vertically consecutive data points. The geostrophic velocity shear $\partial v_g/\partial z$ was calculated from potential density profiles based on UCTD data as

$$\frac{\partial v_g}{\partial z} = -\frac{g}{\rho_0 f}\frac{\partial\overline{\sigma_\theta}}{\partial x}, \tag{4}$$

where g, ρ_0, and f are the gravitational acceleration, reference density (=1025 kg m^{-3}) and inertial frequency, respectively. The gradient Richardson number Ri for the geostrophic field was derived from $\partial v_g/\partial z$, and buoyancy frequency calculated from the smoothed potential density profiles was obtained from UCTD data as:

$$\mathrm{Ri} = \frac{N^2}{\left(\frac{\partial v_g}{\partial z}\right)^2}, \tag{5}$$

Absolute geostrophic velocity was calculated by integrating Eq. (4) and adding a depth-averaged ADCP velocity as:

$$v_g(z) = \int_z^s \frac{\partial v_g}{\partial z}\mathrm{d}z - \frac{1}{s-d}\int_d^s \mathrm{d}z \int_z^s \frac{\partial v_g}{\partial z'}\mathrm{d}z' + \frac{1}{s-d}\int_d^s v_{\mathrm{ADCP}}\mathrm{d}z, \tag{6}$$

where the upper bound s and the lower bound d of the integrals indicate the shallowest and deepest depth of available records, respectively, for either UCTD or ADCP. Although the depth-averaged ADCP velocity data include ageostrophic flows such as tides, we assumed that the north–south components in areas with a bottom depth >100 m as considered here were mostly caused by the geostrophic flows of the TWC and the OY. Assuming that the geostrophic relative vorticity ζ_g along the front between the TWC and the OY was represented by the shear vorticity, we calculated the Rossby number Ro in Eq. (1) as:

$$\mathrm{Ro} = \frac{1}{f}\frac{\partial v_g}{\partial x}. \tag{7}$$

To examine double-diffusive stability, the Turner angle Tu was calculated from the smoothed profiles of potential temperature θ and salinity S obtained from the UCTD data as

$$\mathrm{Tu} = \tan^{-1}\left(\frac{\alpha\frac{\partial\bar{\theta}}{\partial z} + \beta\frac{\partial\bar{S}}{\partial z}}{\alpha\frac{\partial\bar{\theta}}{\partial z} - \beta\frac{\partial\bar{S}}{\partial z}}\right). \tag{8}$$

where α and β are thermal expansion and haline contraction coefficients, respectively (Ruddick 1983).

In addition to the data observed aboard the R/V *Daisan Kaiyo Maru*, data from other sources were also used to consider the linkage between the front and other areas. Data from hydrographic observations off the Sanriku Coast along 40°N, 39°15′N and 38°56′N conducted by the Iwate Fisheries Technology Center over the same period, 8th–10th of July, and bottom temperature and salinity data from mooring systems at the mouth of Otsuchi Bay (Ishizu et al. 2015, submitted) were analyzed.

A sea surface temperature (SST) composite map for the study area was produced from the Moderate Resolution Imaging Spectroradiometer (MODIS) 11 and 12-μm channel SST products. Level 3-mapped SST from the Aqua and Terra satellites, with a horizontal grid interval of ~9 km, averaged from 3 to 10 July 2013 was downloaded from the Ocean Color homepage (http://oceancolor.gsfc.nasa.gov). From four mapped products (daytime and nighttime data each for Aqua and Terra), composite values were estimated at each pixel by taking an ensemble median within a window of 9 pixels (a maximum of 36 values).

3 Results

3.1 Temperature and salinity profiles

The composite SST map for early July 2013 captures narrow bands of warm and cold water off the shelf of the Sanriku Coast from about 39°10′N to 39°50′N, where the shipboard observations of the present study were made (Fig. 1b). The cold water band from 142°20′E to 142°40′E

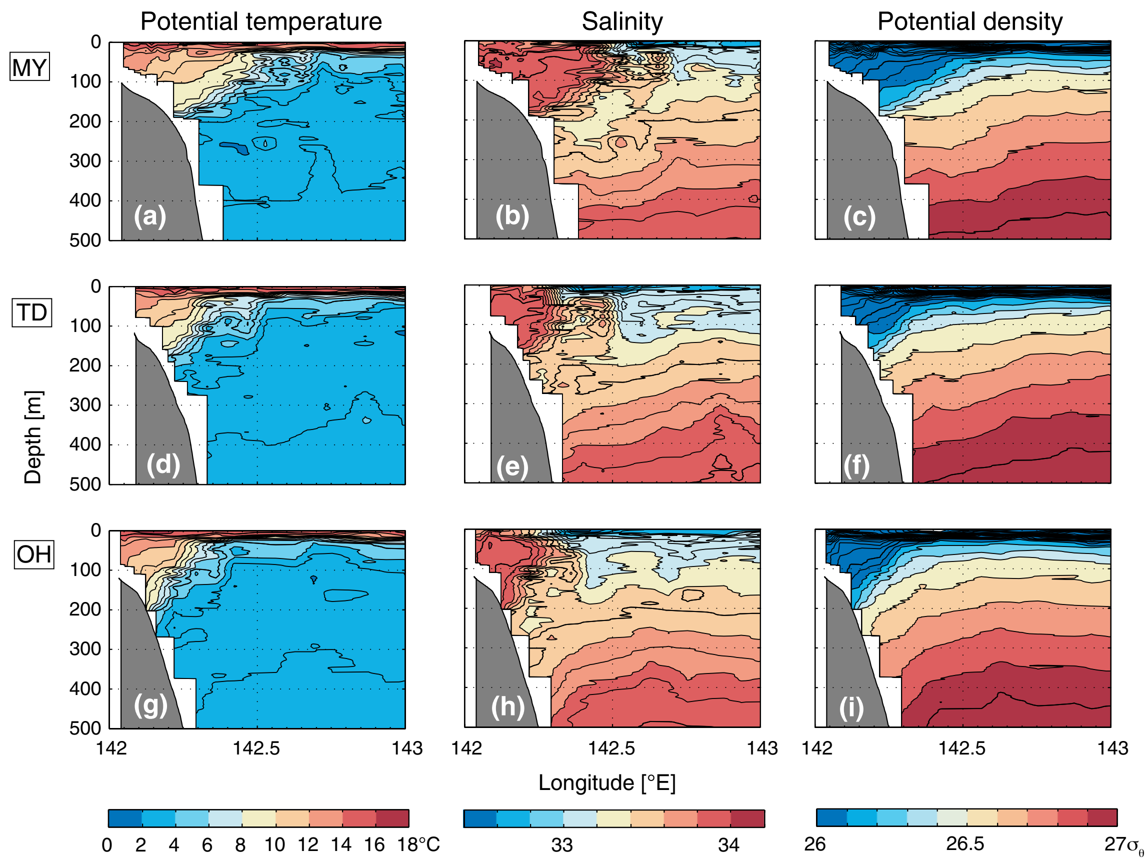

Fig. 2 Cross-sections of potential temperature (*left column*), salinity (*middle column*) and potential density (*right column*) along the MY line (*upper row*), TD line (*middle row*) and OH line (*bottom row*). Intervals for *thin* (*thick*) *contour lines* are 1 °C (5 °C), 0.1 (0.5) and $0.1\sigma_\theta$ $(1.0\sigma_\theta)$ for potential temperature, salinity, and potential density, respectively

was apparently connected to colder water north of 41°N (Fig. 1a), whereas the minimum SST <16 °C was distributed within an area from 39°10′ to 39°50′N. Although large-scale SST features (Fig. 1a) show a clear contrast between this cold water and the warm water from the south, likely originating from the Kuroshio, a relatively warm band with a typical width of 10′–20′ (14–28 km) is also seen west of this cold band. As seen later in the transects (Fig. 2) and a temperature–salinity diagram (Fig. 3), these cold and warm water bands reflect the waters of the OY and TWC, respectively, which are separated more clearly by subsurface water properties.

The potential temperature and salinity sections across the continental shelf observed with the UCTD show clear contrasts between the warm and saline, and the cold and fresh waters, for all the three lines (Fig. 2). In particular, the high horizontal resolution of the observations made it possible to detect the frontal zone as a sharp horizontal gradient in potential temperature and salinity. According to the water classification by Hanawa and Mitsudera (1987), the temperature and salinity of waters in the inshore side of the front is mostly found in the typical temperature/salinity range for the TWC water (warmer than 5 °C and saltier than 33.7 by their definition). Waters categorized as the OY (colder than 7 °C, fresher than 33.7 and lighter than $26.7\sigma_\theta$ by their definition) was found in the offshore side of the front. Small-scale disturbances occurred on the offshore side of the front, interleaving warm/saline and cold/

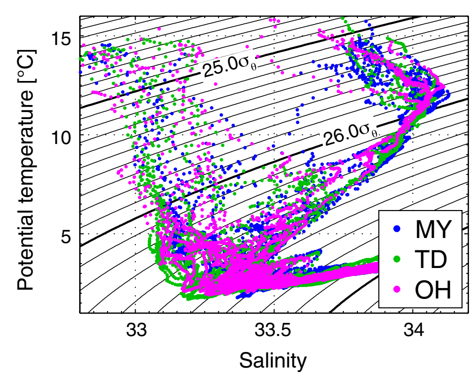

Fig. 3 Temperature–salinity diagram for UCTD data obtained along the three lines. Data below 10 m are shown

fresh waters: these disturbances are hereinafter referred to as frontal disturbances.

The surface layer, strongly stratified in this season, was generally warmer than 15 °C, yet isotherms, isohalines and isopycnals slanted markedly from the subsurface to the bottom of the shelf. Although an along-slope gradient of potential temperature on the bottom was observed up to a depth of 100 m, that of salinity was confined near 200 m, indicating that TWC water occurred above this level (Fig. 2b, e, h). This benthic salinity front lay in a potential density range of about 26.0–26.6σ_θ (Fig. 2c, f, i).

The OY water distributed east of the front was characterized by low potential temperature and salinity. A vertical minimum of potential temperature was observed between the subsurface and about 400 m. Near the surface, the difference in potential temperature between OY water and TWC water was small, as seen in the SST map, but salinity was clearly lower than that in the TWC area (Fig. 2b, e, h).

While the frontal structure along the three lines had the common features mentioned above, there were also some differences. The slope of the front steepened from the north to south. The slope in the lower layer in the OY area water was also steeper in the south than in the north (e.g., Fig. 2g–i). The structure of the frontal disturbances was also different along different lines.

A diagram of potential temperature and salinity (T–S diagram) obtained from UCTD data shows a clear bimodal structure in the layers above 26.6σ_θ (Fig. 3). As seen in Fig. 2, the high-salinity branch represents TWC water and the low salinity branch represents OY water. Although the two branches above 26.1σ_θ were successfully separated by a salinity of 33.7, the boundary of the average range of these water masses proposed by Hanawa and Mitsudera (1987), those in the 26.1–26.6σ_θ layer were better separated by a salinity of 33.3 in our observations.

The salinity of the TWC branch generally increased with increasing temperature from 4 to 12 °C, where it reached its maximum (Fig. 3). From the salinity maximum up to the surface, salinity decreased with increasing temperature. This negative gradient of salinity with depth near the surface is presumably caused by net fresh water input from the surface to the relatively saline TWC water originating from the subtropical gyre. Below the salinity maximum, profiles obtained along the MY line exhibited slightly higher salinity than those along the TD and OH lines. In contrast to the TWC branch, the salinity of the OY branch generally decreased with increasing temperature above 26.6σ_θ. The lowest salinity below 26.0σ_θ was observed along the TD line.

The distributions of potential temperature and salinity between the two distinct branches in the T–S plane are likely the consequences of horizontal and/or vertical mixing of different water masses. Prominent anomalies occurred mainly in the range 26.0–26.6σ_θ. Warm and saline peaks apparently arose on the OY side. This indicates that relatively warm and saline water masses intruded into the 26.0–26.6σ_θ layer toward the OY area with cold and fresh water above and below, forming the frontal disturbances seen in Fig. 2. However, significant intrusion of cold and fresh water toward the TWC area is not observed, except in layers above 25.6σ_θ.

3.2 Velocity structure

Differences in the structure along the three lines are also seen in the horizontal velocity (Fig. 4). East–west components were stronger in magnitude than the north–south components along the MY line except for the area shallower than 100 m, whereas southward flow dominated along the TD and OH lines. The southward flows were concentrated to the coastal side of the front, indicating that the flow was the TWC. The maximum speed exceeded 0.8 m s^{-1} along the OH line (Fig. 4f). The velocity in the Oyashio area was relatively weak, but a southward velocity component of 0.1–0.4 m s^{-1} was widely evident from the front to 142°45′E. Note that the southward flows generally occurred in water columns in which isopycnals were deeper on the coastal side, suggesting the contribution of baroclinic components of the geostrophic flow. The geostrophic velocity structure is shown in the next subsection.

Horizontal distributions of the salinity and velocity at UCTD stations highlight the latitudinal differences in frontal structure (Fig. 5). Along the MY line, convergent zonal flow accelerates the southward flow downstream. The flow structure and longitudinal gradient in salinity broadly follow the bottom topography. High salinity was distributed farther offshore along the MY line where the shelf is wider than on the other two lines (typically seen in distributions of circles in Fig. 5). Also, the westward flow along the MY line apparently followed the bottom topography. As is clear from Fig. 5, the UCTD observations enable us to capture the fine structures associated with the front, while the conventional observations using the CTD (see 40°N and 38°56′N) were too sparse.

Saline waters were observed in the TWC area with maximum salinity exceeding 34.0 at 50 and 100 m, as already seen in Fig. 2. However, salinity at 50 m generally decreased coastward where the water was shallower than 200 m. The decreasing coastward trend of salinity at 50 m was even observed in an inshore area, within Otsuchi Bay, as observed by the mooring system at the bay mouth (41 and 53 m, shown as marks near the coast along 39°21′N in Fig. 5a).

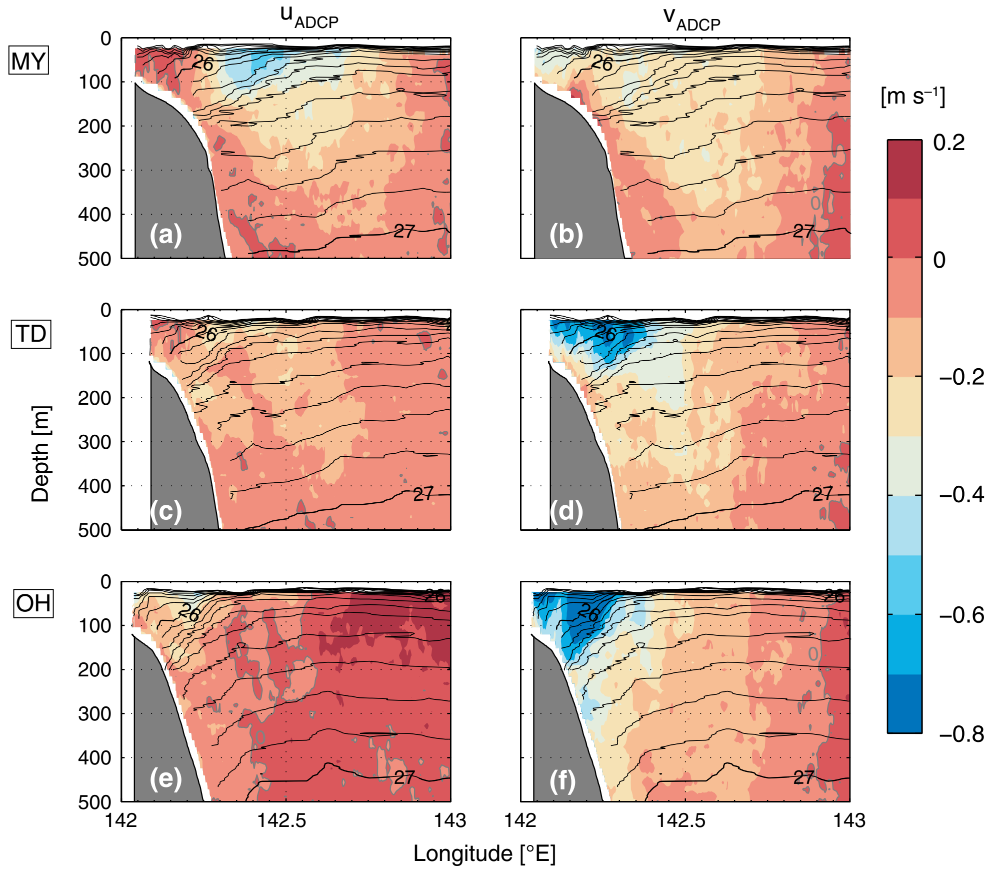

Fig. 4 Cross-sections of horizontal velocity observed with the shipboard ADCP: eastward and northward components are shown in the *left and right columns*, and data along the MY, TD, and OH lines are shown in the *top, middle, and bottom rows*, respectively. *Contour lines* indicate potential density [σ_θ] observed with the UCTD

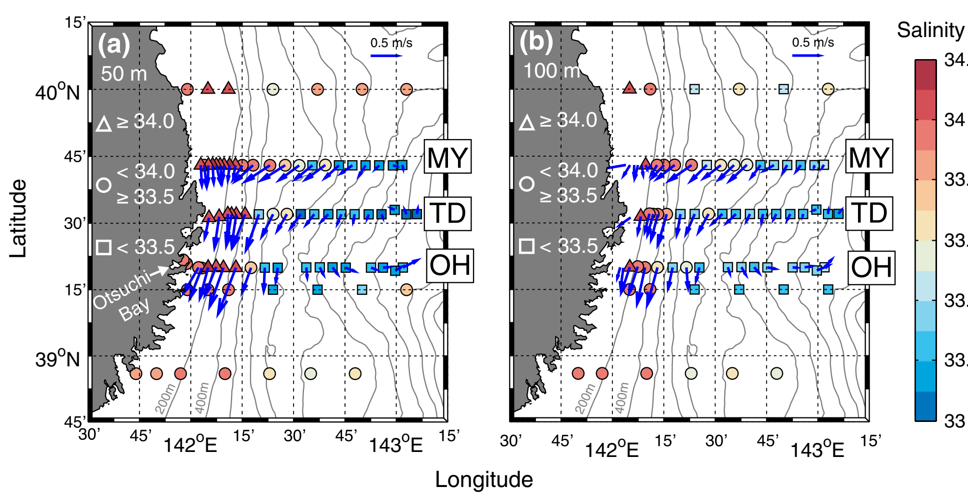

Fig. 5 Distributions of salinity observed with the UCTD (*colored symbols*) and horizontal velocity observed by the shipboard ADCP (*arrows*): at **a** 50 m (56 m for horizontal velocity) and **b** 100 m (104 m for horizontal velocity). **a** Bottom salinity data at the mouth of Otsuchi Bay as retrieved from the two mooring systems at the mouth of Otsuchi Bay (41 and 53 m at the northern and southern parts of the bay mouth, respectively) were also shown. *Squares*, *circles* and *triangles* are used for salinity < 33.5, 33.5 ≤ salinity < 34.0, and 34.0 < salinity, respectively. Bottom depths are indicated by *gray contours* with an interval of 200 m

3.3 Shear and microstructure

The geostrophic velocity shear structure of the TWC and the OY was revealed by the UCTD observations (Fig. 6). Narrow bands of enhanced negative shear with magnitudes exceeding 5×10^{-3} s^{-1} were observed along the front characterized by sharp horizontal gradients in potential temperature and salinity (Fig. 2). The magnitude of the shear was strongest along the OH line where the southward flow of the TWC was most prominent (Figs. 4, 5). Strong negative shear was also found near the coast on the shelf, especially along the OH line. Offshore of the front, the magnitude of the geostrophic velocity shear was relatively moderate; however, negative values of ~10^{-3} s^{-1} were observed along the bottom slope on the OH line, corresponding to the slope of the isopycnals (Fig. 6c).

Distributions of the signed Rossby number Ro and the inverse Richardson number Ri^{-1} are shown in Fig. 7. The values of Ro along the three lines mostly ranged from −0.32 ($-10^{-0.5}$) to 0.32 ($10^{0.5}$), except in coastal areas where tidal flows might have substantial contribution to the depth-averaged ADCP flow (Fig. 7a–c). Magnitudes of Ro were generally high around the front where flows of the TWC and the OY were observed, whereas the signs changed across the flow. As both of the TWC and the OY flowed southward, Ro became negative (positive) due to the anticyclonic (cyclonic) relative vorticity in the western (eastern) side of the flow axis (Fig. 7a–c, see also Fig. 4): negative and positive values of Ro in the inshore flank of the front corresponded to the flow of the TWC, and those from the front to the offshore flank of the front (negative values in intermediate and lower layers from 142°15′ to 142°30′E and positive values in wide areas east of 142°30′E) were caused by the flow of the OY.

Distributions of the inverse Richardson Ri^{-1} indicate that the strong negative shear of the geostrophic velocity observed along the front of the three lines and on the shelf of the OH line was comparable to the buoyancy frequency (Fig. 7d–f). The values of Ri^{-1} ranged from approximately 0.1–1 along the front, and was mostly $O(1)$ along the OH line (Fig. 7c). High Ri^{-1} was also estimated on the shelf for all three lines, again $O(1)$ along the OH line (Fig. 7c), and 0.1–0.3 near the bottom slope of the OH line offshore of the front. For water columns above the bottom layer in the offshore area, Ri^{-1} was relatively low compared to that for the inshore side of the front, with a typical range of 0.001–0.01, although slight elevations were observed in some parts of water columns west of 142°45′E.

According to Eq. (1), the minimum frequency of internal waves ω_{min} is estimated from Ro and Ri^{-1} (Fig. 8). The values of Ro–Ri^{-1} became negative for wide areas around the front along the MY line (Fig. 8a) and for coastal sides and lower parts of the front along the TD and OH lines

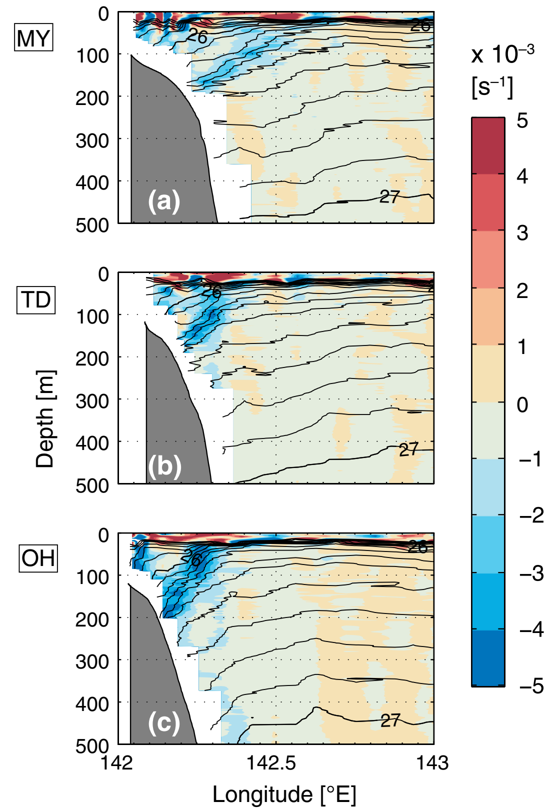

Fig. 6 Vertical shear of geostrophic velocity calculated from the UCTD data. Values greater (smaller) than 5×10^3 (-5×10^3) s^{-1} are shown with a same color as 4 to 5×10^3 (−5 to -4×10^3) for visibility. *Contour lines* indicate potential density

(Fig. 8b, c). This caused decreases in ω_{min} from the inertial frequency and, hence, increases in the maximum periods of the internal waves to exist, from the inertial period of 18.9 h (Fig. 8d–f). The maximum period widely exceeded 20 h in the frontal area along the MY line with the maximum values above 22 h in a 50–150 m layer (Fig. 8a). Along the TD and OH lines, increases in the maximum period did not occur widely in the frontal area but markedly high patches were observed in the coastal sides and lower pars of the front. It is noted that these values exceeded 24 h, suggesting that internal waves with a diurnal frequency could locally exist.

The vertical shear of ADCP horizontal velocity reflected not only the synoptic structure of the TWC and the OY but also the smaller-scale disturbances (Fig. 9). Besides the bands of negative shear corresponding to the TWC (Fig. 6), streaks of strong positive and negative shear were observed running upward and downward from the shelf break around 200 m. Considering that similar streak patterns observed around the Kuroshio flowing along a shelf margin were attributed to internal waves (Rainville and Pinkel 2004), we assumed that these patterns were caused by the propagation of internal waves that were possibly excited at the shelf break through interactions between currents (either

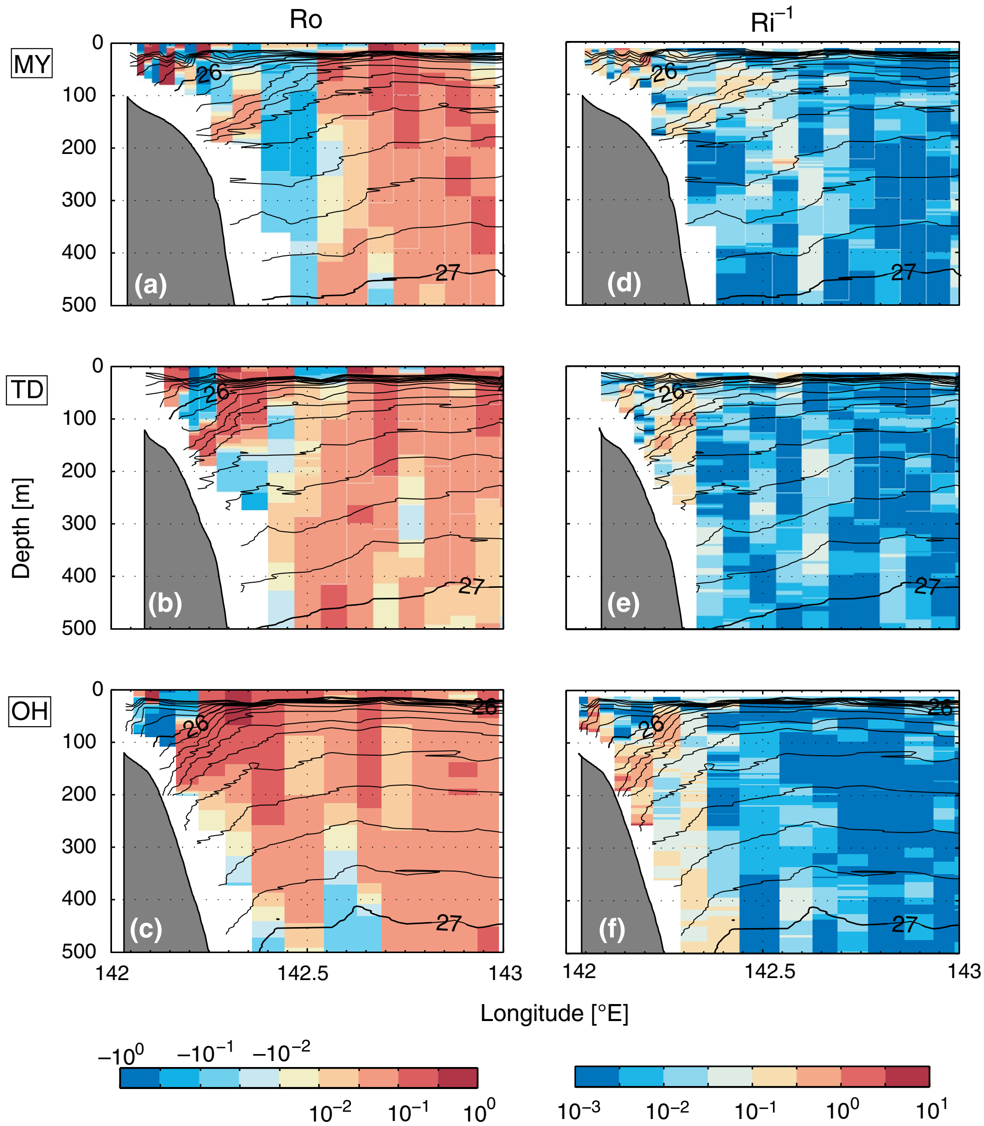

Fig. 7 Rossby number (**a**–**c**) and inverse Richardson number (**d**–**f**) as calculated from the geostrophic velocity and buoyancy frequency. *Color scales* are limited as in Fig. 6. *Contour lines* indicate potential density

tide, TWC or OY) and topography. The amplitudes of some of these streaks exceeded 0.01 s^{-1} (the upper bound of the color scale for Fig. 9 is limited to 0.005 s^{-1} for visibility). The slope of the strongest shear band along the front was less steep than internal waves with a semidiurnal frequency (green lines), indicating a lower intrinsic frequency. As seen in Fig. 8, internal waves with a frequency substantially lower than the inertial frequency could exist only within this shear band along the front. However, specifying the frequency of internal waves that were possibly reflected and trapped within these layers is difficult. The frontal disturbances observed in the temperature and salinity profiles (Fig. 2) were not evident in Fig. 9, indicating the greater contribution of internal waves to the shear field.

Turbulent energy dissipation rates ε and vertical diffusivity K_ρ are shown in Fig. 10. For most profiles below the shallow pycnocline, values of ε were below 10^{-9} W kg^{-1} (Fig. 10a, c, e). Nevertheless, patches of elevated ε with typical magnitudes of 3×10^{-9} to 3×10^{-8} W kg^{-1}were observed even within water columns below the surface pycnocline. Although distributions of the elevated ε were not continuous, they were frequently observed along the front and its eastern (OY) side: along the 26.2–26.4σ_θ isopycnals for the MY line (70–120 m, Fig. 10a), the 26.2–26.4σ_θ isopycnals for the TD line (80–170 m, Fig. 10c) and the 26.0–26.4σ_θ isopycnals for the OH line (80–180 m, Fig. 10e).

An exceptionally strong ε was observed closest to the coast in the VMP deployment along the OH line. The

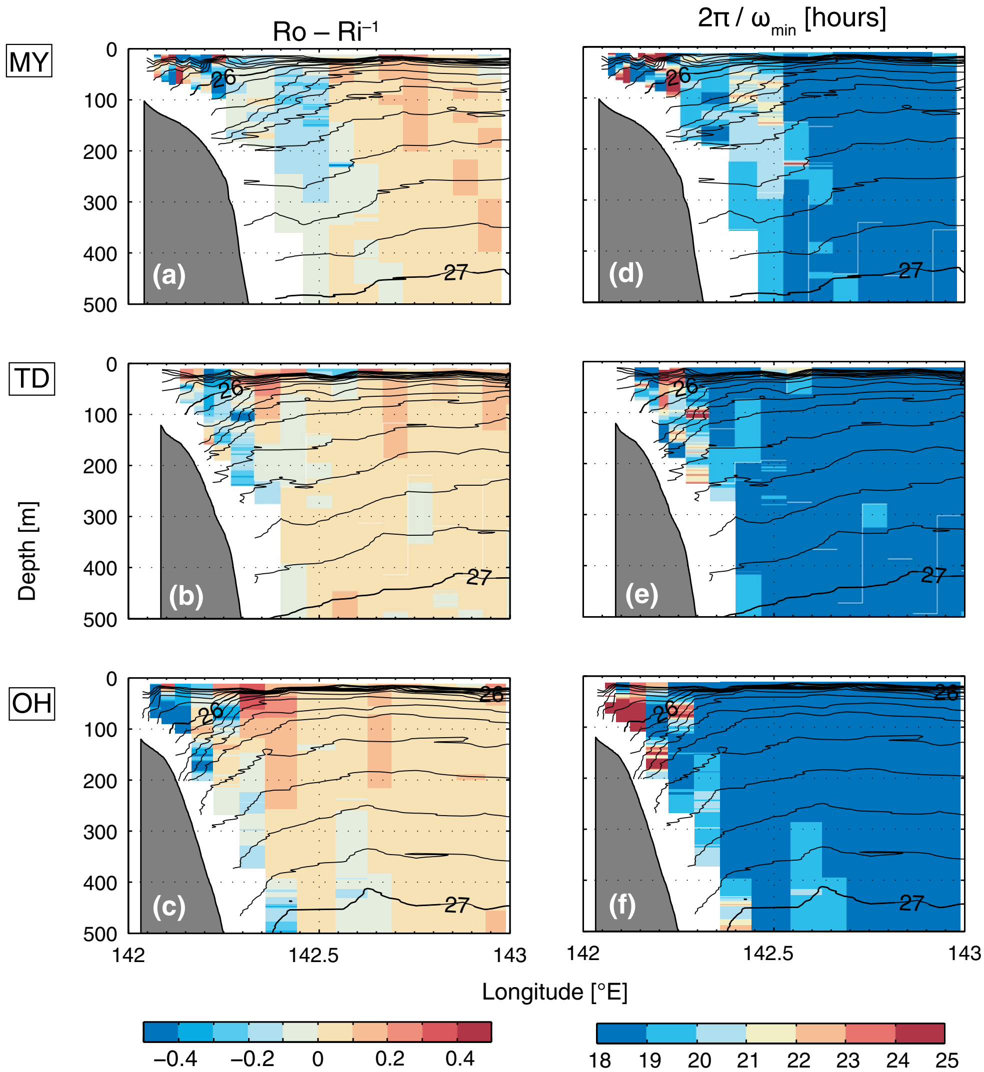

Fig. 8 Distributions of Ro–Ri^{-1} (**a–c**) and $2\pi/\omega_{\mathrm{min}}$ (maximum frequency for internal waves to exist) (**d–f**). *Color scales* are limited as in Fig. 6. *Contour lines* indicate potential density

values were above 10^{-7} W kg^{-1} from 50 to 80 m, with the maximum exceeding 10^{-6} W kg^{-1} at 80 m (Fig. 10c). Note that three VMP casts were made at this station, yielding similar estimates of ε (only the results of the first cast are shown in Fig. 9).

Vertical diffusivity mostly ranged from 3×10^{-6} to 1×10^{-4} m^2 s^{-1} (Fig. 10b, d, f). The highest level of ~10^{-4} m^2 s^{-1} occurred partly along the front where ε was also strong, but the distribution was not coincident because of the contribution of N^2. The exceptionally strong ε right at the coastal end of the OH line yielded a vertical diffusivity >10^{-3} m^2 s^{-1}, with a maximum >10^{-2} m^2 s^{-1} (Fig. 10f).

In addition to the enhanced energy dissipation caused by turbulence, water columns near the front are also susceptible to double diffusion (Fig. 11). The water columns inshore of the front, mainly consisting of TWC water, generally had upward gradients in salinity and temperature, and were, thus, preferred sites for salt-finger convection as indicated by the Turner angle (Tu > 45°) (Fig. 11a, c, e). Along the eastern side of the front, however, layers favoring salt-finger convection and those favoring diffusive convection (Tu < −45°) occurred close together within a thickness of several tens of meters, due to the interleaving structure of temperature and salinity (Fig. 2). Note that the magnitude of Tu in these layers frequently exceeded 60°, indicating strong preferences for either salt-finger or diffusive convection. Further offshore, water columns mostly favored double diffusive convection; however, the strong preference for |Tu| > 60° was not as marked as in the frontal area.

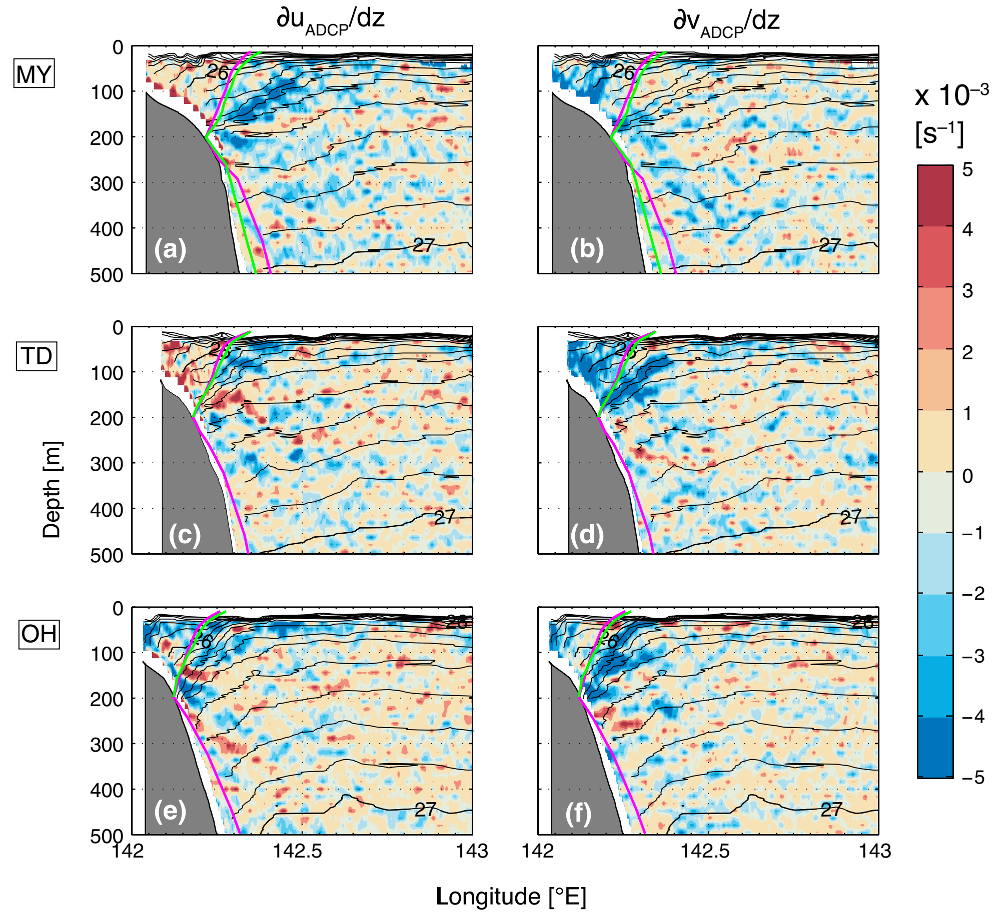

Fig. 9 Vertical shear of horizontal velocity observed with the shipboard ADCP. *Green and magenta lines* indicate characteristics of M_2 internal waves based on the linear theory and the formulation derived by Whitt and Thomas (2013), respectively (nearest values of stratification and shear data were used to conduct calculations near the bottom). *Contour lines* indicate potential density

Profiles of vertical temperature gradient measured with a high-resolution FP07-38 thermistor attached to the VMP are shown in Fig. 11b, d, and f. Water columns with strong temperature variation primarily corresponded to those with strong turbulence (Fig. 10). Nevertheless, there were layers with relatively strong temperature variations but with weak turbulence. These layers were mostly found below the pycnocline. In some of these layers, the variations had either positive or negative prominent peaks within a thickness of $O(10\text{ m})$, which is indicative of the step-like structure caused by double diffusion, as suggested by Inoue et al. (2007).

4 Discussion and conclusions

4.1 Mechanisms for enhanced vertical mixing

Observations using UCTD and shipboard ADCP have revealed the fine structure in the front between the TWC and the OY off the Sanriku Coast. A strong horizontal gradient in water properties, especially salinity, was observed along the front from the subsurface onto the shelf. The magnitude of the geostrophic shear was markedly elevated, in some places exceeding $5 \times 10^{-3}\ \text{s}^{-1}$, comparable to observations along the Kuroshio (Fig. 6; Kaneko et al. 2012; Nagai et al. 2009, 2012; Rainville and Pinkel 2004). In consequence, the inverse Richardson number Ri^{-1} for the geostrophic field became $O(1)$ along the front (Fig. 7).

High turbulent energy dissipation rates ε up to $3 \times 10^{-8}\ \text{W kg}^{-1}$ were frequently observed along the front. We consider two factors to be responsible for this strong turbulence. The first one is the generation of tidally driven internal waves. As seen in Fig. 9, a beam-like structure apparently emanated from the shelf break in both upward and downward directions. Although the energy inputs from the propagating internal waves may be directly related to dissipation, the more frequent occurrences of high ε along the front suggest the second factor: i.e., trapping and amplification of internal waves within a sheet of high geostrophic velocity shear.

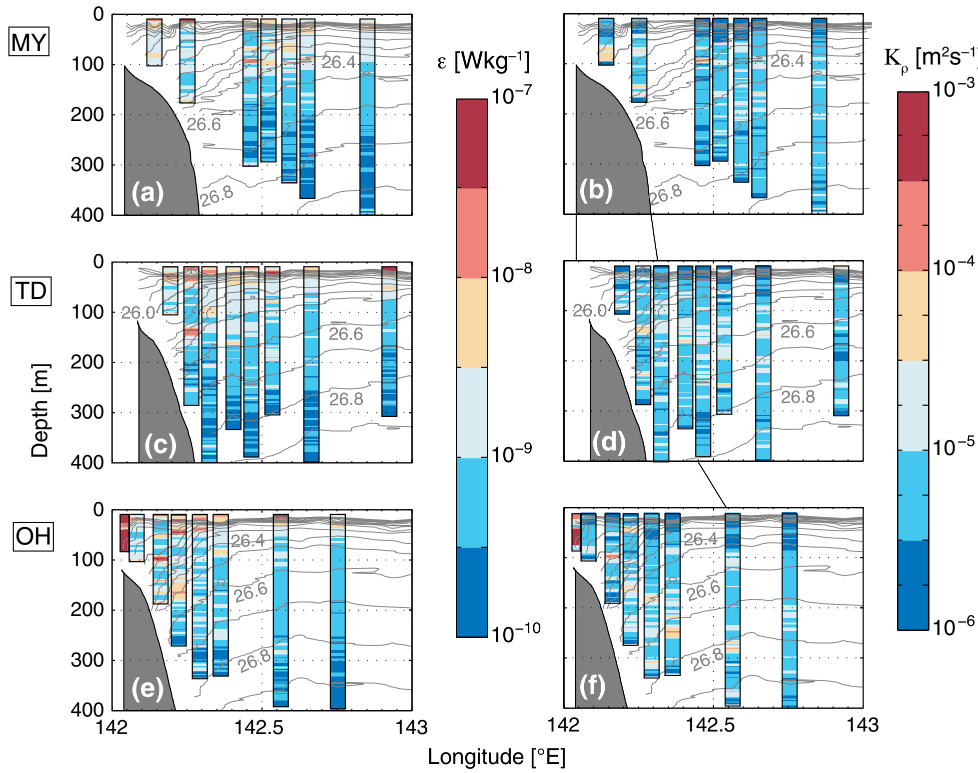

Fig. 10 Turbulent energy dissipation rates (*left column*) and vertical diffusivity (*right column*). *Gray contour lines* indicate potential density

As seen in Fig. 8, substantial decreases in the minimum frequency $\omega_{\min}$ (increases in the maximum periods) for internal waves were observed around the front. In particular, markedly high period patches exceeding 24 h were observed in the coastal side and the lower parts of the front along the TD and OH lines, which was caused by the high Ri^{-1} of $O(1)$. The effect of the shear on the dispersion relation of internal waves, however, depends on the propagation direction of the waves. According to Whitt and Thomas (2013), the dispersion relation in a strong eastward baroclinic current is derived as (their Eq. 42)

$$\omega = \sqrt{F^2 + 2f(\partial u_g/\partial z)\alpha + N^2\alpha^2} \tag{9}$$

where the effective inertial frequency $F = [f \times (f + \zeta_g)]^{1/2}$ (their Eq. 18) and $\alpha = l/m$ is the ratio of the northward and upward components of the wave number vector. Rotating the frame of reference by 90° clockwise for the present study, we have

$$\omega = \sqrt{F^2 - 2f(\partial v_g/\partial z)(k/m) + N^2(k^2/m^2)}, \tag{10}$$

where k is the eastward component of the wave number vector. Since $\partial v_g/\partial z$ was generally negative around the front (Fig. 6), a negative k/m will decrease ω. This condition is satisfied for upward offshore energy radiation from the shelf break, which can follow the strong geostrophic shear band of the front. The minimum frequency, as in Eq. (1), is obtained when $k/m = f/N^2(\partial v_g/\partial z)$.

Unlike wind stress that has a relatively wide frequency range, major tidal forcing generally has either a semidiurnal or diurnal frequency. Consequently, the energy of internal tides is primarily concentrated around semidiurnal and diurnal frequencies. In the present study, at 39°30′N, the semidiurnal tide is superinertial but the diurnal tide is sub-inertial. The internal tide with diurnal frequency can propagate vertically only when $\omega_{\min} < \omega_{\mathrm{diurnal}}$. As seen in Fig. 8, internal waves with diurnal frequency could exist within the lower part of the strong shear band of the front, which may have enhanced the turbulence. We term this effective energy transfer from the tidal forcing to the upper layer the "internal tide chimney", by analogy with the inertial chimney that transfers atmospheric energy to the deep layer as proposed by Lee and Niiler (1998).

Interaction between tide and high topography can generate internal waves with a frequency not identical to tidal frequencies but that are scaled with the shape of the topography and the stratification (Klymak et al. 2010; Itoh et al. 2014). This suggests that even a layer with a minimum frequency of $\omega_{\mathrm{diurnal}} < \omega_{\min} < f$, as the frontal layer along the MY line, can potentially trap energy generated by tide,

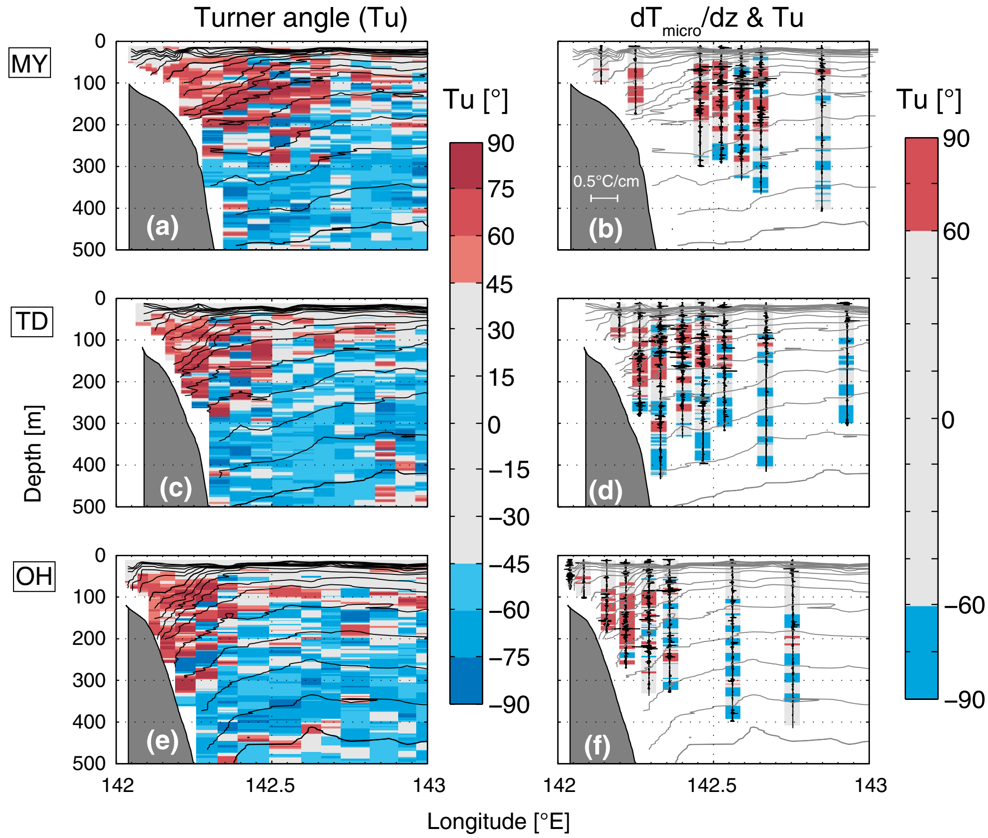

Fig. 11 Turner angle Tu calculated from UCTD data (*left column*) and vertical shear of temperature obtained from a microstructure thermistor (*right column*). Values in the range $-45° < \mathrm{Tu} < 45°$ are shown in *light gray* to highlight water columns with $|\mathrm{Tu}| > 45°$. *Contour lines* indicate potential density

although we could not examine frequencies of generated waves from the present data.

As reviewed in Sect. 1, formulations by Whitt and Thomas (2013) (Eqs. (1), (9) and (10) in the present study) were valid at least qualitatively for internal waves with scales not so much greater than flow scale. The behavior of larger-scale internal waves was likely different from our prediction based on the above equations. Therefore, we assume that small- and moderate-scale internal waves compared to the front scale contribute to the internal tide chimney.

The internal tide chimney may develop if a coastal boundary current flows with the coast to its right (left) in the northern (southern) hemisphere. This is the case for the TWC (e.g., Takikawa et al. 2005) and the Soya Warm Current (SWC; e.g., Ishizu et al. 2008) in the waters around Japan. The Leeuwin Current in the Indian Ocean (e.g., Koslow et al. 2008), the Norwegian Coastal Current in the North Atlantic (e.g., Skagseth et al. 2011) and the Aleutian North Slope Current in the Bering Sea (Stabeno et al. 2009) also meet this condition. Examination of the applicability of internal tide chimney processes will be made in future studies.

The internal tide chimney cannot explain the exceptionally strong mixing observed at the coastal end of the OH line. This is more likely to be driven by the wind forcing and direct influences of tidal forcing, such as bottom friction and breaking of large-amplitude internal waves (Masunaga et al. 2015, this issue; Sakamoto et al. 2015, submitted).

4.2 Frontal variability along the front and impacts on ecosystems

An important effect of vertical mixing on the ecosystem is upward nutrient transport, which induces increased primary production in the photic layer. Although we did not make observations of nutrient concentration, an observation on 27 June 2013 suggests elevated productivity around the front (Fig. 12). It was made along 39°20′N, almost along the OH line of the present study, during cruise KK-13-01 of R/V *Daisan Kaiyo Maru*. A high concentration of chlorophyll *a* fluorescence was observed at subsurface layers of a station at 142°30′E, where the front was observed in July. The maximum value was 3.6 mg m^{-3} at a 20-m depth,

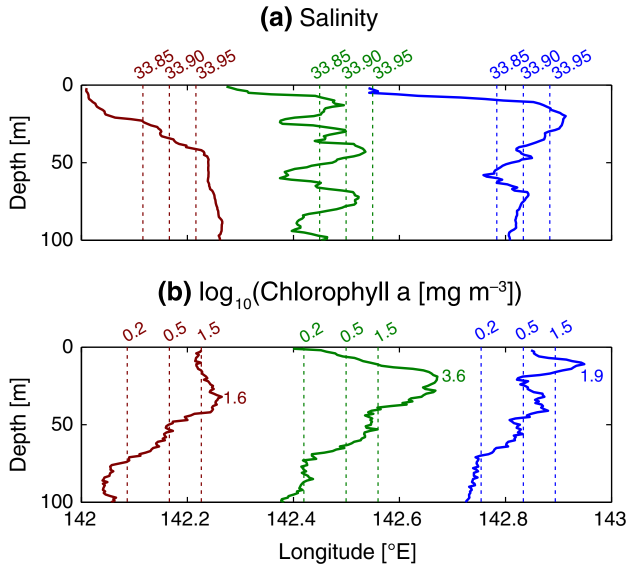

Fig. 12 Vertical profiles of **a** salinity and **b** chlorophyll *a* fluorescence as observed with a CTD during cruise KK-13-1 of R/V *Daisan Kaiyo Maru*

twice as high as those of the inshore profile at 142°10′E (1.6 mg m^{-3} at 32 m) and the offshore profile at 142°50′E (1.9 mg m^{-3} at 11 m). It is suggested that enhanced turbulence in the lower layer of the front supplied nutrients to the subsurface layer.

Mixing around the front may occur not only vertically but also horizontally, and also through double diffusion. In particular, the disturbances widely observed in the 26.0–26.6σ_θ layers (Figs. 2, 3) may enhance effective horizontal and vertical mixing, resulting in modification of water masses. It was observed that salinity of the core TWC water has a southward decreasing trend (Fig. 3). It is likely that the core of the TWC becomes cold, fresh and eutrophic due to horizontal and vertical mixing as it flows southward.

The disturbances and mixing around the front may also influence the migration of demersal species on the shelf. It is known that North Pacific giant octopuses migrate into shallow shelf areas off the Sanriku Coast in summer. Since they are mainly found in coastal areas of Hokkaido where the water is colder, their seasonal southward migration should occur first along the southward extension of the cold OY water. The disturbances and mixing around the front may encourage the North Pacific giant octopus and other cold-water species to follow the shallow shelf. It is also likely that enhanced primary production along the front causes aggregations of various demersal and pelagic species.

Although the present study focuses on the front between the TWC and the OY, modification of the TWC can also impact the inner bays. While there are many bays along the Sanriku Coast (Fig. 1b), the southward gradient in water properties of the TWC influencing the circulation of the bays (e.g., Ishizu et al. 2015; Sakamoto et al. 2015) should cause a gradient in biota and productivity in the bays. Interactions between waters of the TWC, the OY and the inner bays will be examined in future studies through ongoing observations and numerical experiments for this area.

Acknowledgments This research was supported by the Tohoku Ecosystem-Associated Marine Sciences (TEAMS) by the Ministry of Education, Culture, Sports, Science and Technology in Japan. S. Itoh, H. Kaneko and T. Okuhishi were also supported by The New Ocean Paradigm on its Biogeochemistry, Ecosystem, and Sustainable Use (NEOPS). The authors thank S. Kouketsu, H. Kawahara and I. Yasuda for preparation and deployments of the UCTD profiler. The data obtained by R/V *Daisan Kaiyo Maru* are available on the Research Information and Data Access Site of TEAMS (RIAS). The data from the Iwate Fisheries Technology Center are available on its website (http://www2.pref.iwate.jp/~hp5507/).

References

Conlon DM (1982) On the outflow modes of the Tsugaru Warm Current. La mer 20:60–64

D'Asaro E, Lee C, Rainville L, Harcourt R, Thomas L (2011) Enhanced turbulence and energy dissipation at ocean fronts. Science 332(6027):318–322

Hanawa K, Mitsudera H (1987) Variation of water system distribution in the Sanriku coastal area. J Oceanogr Soc Jpn 42:435–446

Inoue R, Gregg MC, Harcourt RR (2010) Mixing rates across the Gulf Stream, part 1: on the formation of Eighteen Degree Water. J Mar Res 68(5):643–671

Inoue R, Yamazaki H, Wolk F, Kono T, Yoshida J (2007) An estimation of buoyancy flux for a mixture of turbulence and double diffusion. J Phys Oceanogr 37(3):611–624. doi:10.1175/jpo2996.1

Ishizu M, Itoh S, Tanaka K, Komatsu K (2015) Influences of the Tsushima and Oyashio Currents on the circulation and water properties of Otsuchi Bay. J Oceanogr (submitted)

Ishizu M, Kitade Y, Matsuyama M (2008) Characteristics of the cold-water belt formed off Soya Warm Current, J Geophys Res 113(C12). doi:10.1029/2008jc004786

Itoh S, Sugimoto T (2002) Direct current measurements off Sanriku, east of Japan. J Oceanogr 58(6):877–882. doi:10.1023/A:1022883415672

Itoh S, Yasuda I, Nakatsuka T, Nishioka J, Volkov YN (2010) Fine- and microstructure observations in the Urup Strait, Kuril Islands, during August 2006. J Geophys Res 115. doi:10.1029/2009JC005629

Itoh S, Tanaka Y, Osafune S, Yasuda I, Yagi M, Kaneko H, Konda S, Nishioka J, Volkov YN (2014) Direct breaking of large-amplitude internal waves in the Urup Strait. Prog Oceanogr 126:109–120. doi:10.1016/J.Pocean.2014.04.014

Johnston TMS, Rudnick DL, Pallas-Sanz E (2011) Elevated mixing at a front. J Geophys Res 116(C11). doi:10.1029/2011jc007192

Joyce TM (1989) On in situ "calibration" of shipboard ADCPs. J Atmos Ocean Technol 6(1):169–172. doi:10.1175/1520-0426(1989)006<0169:oisosa>2.0.co;2

Kaneko H, Yasuda I, Komatsu K, Itoh S (2012) Observations of the structure of turbulent mixing across the Kuroshio. Geophys Res Lett 39(15). doi:10.1029/2012gl052419

Kaneko H, Yasuda I, Komatsu K, Itoh S (2013) Observations of vertical turbulent nitrate flux across the Kuroshio. Geophys Res Lett 40(12):3123–3127. doi:10.1002/Grl.50613

Klymak JM, Legg SM, Pinkel R (2010) High-mode stationary waves in stratified flow over large obstacles. J Fluid Mech 644:321. doi:10.1017/s0022112009992503

Koslow JA, Pesant S, Feng M, Pearce A, Fearns P, Moore T, Matear R, Waite A (2008) The effect of the Leeuwin Current on phytoplankton biomass and production off Southwestern Australia. J Geophys Res 113(C7). doi:10.1029/2007jc004102

Kunze E (1985) Near-inertial wave-propagation in geostrophic shear. J Phys Oceanogr 15(5):544–565

Lee DK, Niiler PP (1998) The inertial chimney: the near-inertial energy drainage from the ocean surface to the deep layer. J Geophys Res 103(C4):7579–7591. doi:10.1029/97jc03200

Masunaga E, Fringer O, Yamazaki H (2015) An observational and numerical study of river plume dynamics in Otsuchi Bay, Japan. J Oceanogr. doi:10.1007/s10872-015-0324-2

Nagai T, Tandon A, Yamazaki H, Doubell MJ (2009) Evidence of enhanced turbulent dissipation in the frontogenetic Kuroshio Front thermocline. Geophys Res Lett 36. doi:10.1029/2009GL038832

Nagai T, Tandon A, Yamazaki H, Doubell MJ, Gallager S (2012) Direct observations of microscale turbulence and thermohaline structure in the Kuroshio Front. J Geophys Res 117(C8):C08013. doi:10.1029/2011jc007228

Osborn TR (1980) Estimates of the local-rate of vertical diffusion from dissipation measurements. J Phys Oceanogr 10(1):83–89

Rainville L, Pinkel R (2004) Observations of energetic high-wavenumber internal waves in the Kuroshio. J Phys Oceanogr 34(7):1495–1505

Ruddick B (1983) A practical indicator of the stability of the water column to double-diffusive activity. Deep Sea Res Part A Oceanogr Res Pap 30(10):1105–1107. doi:10.1016/0198-0149(83)90063-8

Rudnick DL, Klinke J (2007) The underway conductivity–temperature–depth instrument. J Atmos Ocean Technol 24(11):1910–1923. doi:10.1175/jtech2100.1

Sakamoto T, Urakawa LS, Hasumi H, Ishizu M, Itoh S, Tanaka K (2015) Numerical simulation of Pacific water intrusions into Otsuchi Bay, northeast of Japan, with a nested-grid OGCM. J Oceanogr (submitted)

Shimizu Y, Yasuda I, Ito S (2001) Distribution and circulation of the coastal Oyashio intrusion. J Phys Oceanogr 31(6):1561–1578

Skagseth Ø, Drinkwater KF, Terrile E (2011) Wind- and buoyancy-induced transport of the Norwegian Coastal Current in the Barents Sea. J Geophys Res 116(C8). doi:10.1029/2011jc006996

Stabeno PJ, Ladd C, Reed RK (2009) Observations of the Aleutian North Slope Current, Bering Sea, 1996–2001. J Geophys Res 114(C5). doi:10.1029/2007jc004705

Takikawa T, Yoon JH, Cho KD (2005) The Tsushima warm current through Tsushima Straits estimated from ferryboat ADCP data. J Phys Oceanogr 35(6):1154–1168. doi:10.1175/jpo2742.1

Wagawa T, Kuroda H, Ito S-I, Kakehi S, Yamanome T, Tanaka K, Endoh Y, Kaga S (2015) Variability in water properties and predictability of sea surface temperature along Sanriku coast, Japan. Cont Shelf Res 103:12–22. doi:10.1016/j.csr.2015.04.016

Whitt DB, Thomas LN (2013) Near-inertial waves in strongly baroclinic currents. J Phys Oceanogr 43(4):706–725. doi:10.1175/jpo-d-12-0132.1

Yasuda I (2003) Hydrographic structure and variability in the Kuroshio–Oyashio Transition Area. J Oceanogr 59(4):389–402

Yasuda I, Okuda K, Hirai M, Ogawa Y, Kudoh H, Fukushima S, Mizuno K (1988) Short-term variations of the Tsugaru Warm Current in autumn (in Japanese with English abstract). Bull Tohoku Reg Fish Res Inst 50:153–191

Zhai X, Johnson HL, Marshall DP (2010) Significant sink of ocean-eddy energy near western boundaries. Nat Geosci 3(9):608–612. doi:10.1038/ngeo943